Simultaneous Enhancement of Efficiency and Operational-Stability of Mesoscopic Perovskite Solar Cells *via* Interfacial Toughening

In Seok Yang, Zhenghong Dai, Anush Ranka, Du Chen,
Kai Zhu, Joseph J. Berry, Peijun Guo, and Nitin P. Padture*

I.S. Yang, Z. Dai, A. Ranka, N.P. Padture
School of Engineering, Brown University
Providence RI 02912, USA
*Email: nitin_padture@brown.edu

D. Chen, P. Guo
Department of Chemical and Environmental Engineering
Yale University
New Haven CT 06520, USA

D. Chen, P. Guo
Energy Sciences Institute
Yale University
West Haven CT 06516, USA

K. Zhu
Chemistry and Nanoscience Center, National Renewable Energy Laboratory,
Golden, CO 80401, USA

J.J. Berry
Materials Science Center, National Renewable Energy Laboratory,
Golden, CO 80401, USA

J.J. Berry
Department of Physics
University of Colorado
Boulder, CO 80309, USA

Keywords: perovskites; solar cells; mesoscopic; interfaces; self-assembled monolayers; stability; mechanical reliability

Abstract

We have investigated the combined effects of compact TiO_2 (c-TiO_2) electron-transport layer (ETL) without and with mesoscopic TiO_2 (m-TiO_2) on top, and without and with an iodine-terminated silane self-assembled monolayer (SAM), on the mechanical behavior, opto-electronic properties, photovoltaic (PV) performance, and operational-stability of solar cells based on metal-halide perovskites (MHPs). The interfacial toughness increases almost three-fold in going from c-TiO_2 without SAM to m-TiO_2 with SAM. This is attributed to the synergistic effect of the m-TiO_2/MHP nanocomposite at the interface and the enhanced adhesion afforded by the I-terminated silane SAM. The combination of m-TiO_2 and SAM also offers a significant beneficial effect on the photocarriers extraction at the ETL/MHP interface, resulting in perovskite solar cells (PSCs) with power-conversion efficiency (PCE) of over 24% and 20% for 0.1 cm^2 and 1 cm^2 active areas, respectively. These PSCs also have exceptionally long operational-stability lives: extrapolated *T*80 (duration at 80% initial PCE retained) is about 18,000 h and 10,000 h for 0.1 cm^2 for 1 cm^2 active areas, respectively. *Postmortem* characterization and analyses of the operational-stability-tested PSCs were performed to elucidate the possible mechanisms responsible for the long operational-stability.

ToC Text and Graphic

The incorporation of self-assembled monolayer (SAMs) at the interface in mesoscopic perovskite solar cells (PSCs) results in unprecedented simultaneous enhancement of mechanical reliability, operational-stability, and power-conversion efficiency (PCE). The three-fold increase in the interfacial toughness in a PSC with a PCE of over 24% is responsible for *T*80 (duration at 80% initial PCE retained) of about 18,000 h. The possible mechanisms responsible for the long operational-stability are elucidated.

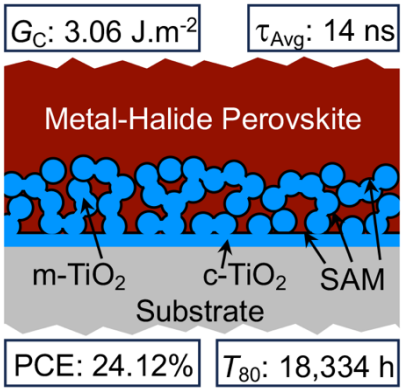

1. Introduction

Tremendous progress has been made over the past decade in enhancing the power-conversion efficiency (PCE), operational-stability, and scalability of perovskite solar cells (PSCs) based on metal-halide-perovskite (MHP) thin-film light absorbers.[1-3] However, progress in mechanical reliability, which is also critically important for the overall durability of PSCs, has been limited.[4-10] While there have been reports on enhancing adhesion toughness of interfaces in PSCs,[4, 7, 11-21] recently we demonstrated a direct correlation between mechanical reliability, and both PCE and operational-stability in planar *n-i-p* rigid PSCs.[22] This was accomplished by significantly increasing the adhesion toughness of the interface between the SnO_2 electron-transport layer (ETL) and the MHP thin film using a iodine-terminated silane-based self-assembled monolayer (SAM) — so-called 'molecular glue.'[22] In a related study, simultaneous enhancement in the PCE, operational stability, and cyclic-fatigue life was achieved in planar *n-i-p* flexible PSCs on plastic substrates.[23] In that case, both interfaces, ETL/MHP and hole-transport layer (HTL)/MHP, were reinforced. The former was achieved by using the SAM,[22] and the latter by using an *in-situ*-grown low-dimensional (LD) MHP at the HTL/MHP interface.[24]

While it is generally known that the use of mesoscopic ETL can improve the adhesion toughness,[14] here we show that the use of mesoscopic TiO_2 (m-TiO_2) atop the compact TiO_2 (c-TiO_2) ETL, together with the SAM, results in unprecedented simultaneous enhancement in mechanical reliability, operational-stability, and PCE in rigid mesoscopic *n-i-p* PSCs. The PCEs of the 'champion' PSCs of 0.1 cm^2 and 1 cm^2 active areas, with both ETL/MHP and HTL/MHP interfaces reinforced, are 24.12% and 20.78%, respectively, and the corresponding extrapolated *T*80 (duration at 80% initial PCE retained) operational-stabilities are 18,334 h and 9,947 h. The correlations between the enhancements in the mechanical properties and both PCE and operational-stability in these PSCs are elucidated.

2. Results and Discussion

2.1. Mechanical Behavior

The interfacial adhesion toughness (G_C) was measured for a set of 'model' interfaces using the 'sandwich' double-cantilever beam (DCB) test method (Fig. 1a),[4, 14, 22] and it is described in the Experimental Section. The following four types of ETL/MHP interfaces were fabricated on commercially obtained glass substrates, and are depicted schematically in Figs. 1b-1e: (i) c-TiO_2/MHP, (ii) c-TiO_2/SAM/MHP, (iii) c-TiO_2/m-TiO_2/MHP, and (iv) c-TiO_2/m-

TiO_2/SAM/MHP. Here c-TiO_2 is compact TiO_2 (~50 nm thickness), m-TiO_2 is mesoscopic TiO_2 (~170 nm thickness), SAM is (3-iodopropyl)trimethoxysilane ($Si(OCH_3)_3(CH_2)_3I$), and the MHP thin film (~600 nm thickness) is of nominal composition $MA_{0.02}FA_{0.98}Pb(Br_{0.02}I_{0.98})_3$. The corresponding G_C values for these interfaces are plotted in Fig. 1f. The white lines/curves and red arrows in Figs. 1b-1e show the fracture paths, as confirmed by characterizing the mating fracture surfaces using scanning electron microscopy (SEM) observations and X-ray photoelectron spectroscopy (XPS), which are presented in Figs. S1-S4 in the Supporting Information (SI). The c-TiO_2/MHP interface is the most brittle (G_C 1.08±0.51 J.m^{-2}), and the fracture occurs cleanly at the interface, as seen in Fig. S1. The SEM image of the MHP side of the fracture surface in Fig. S1a shows the MHP microstructure (grain-boundary grooves), and little evidence of Ti in the corresponding XPS spectrum (Fig. S1b). The ETL side of the fracture surface is relatively smooth and it shows no evidence of MHP (Figs. S1c and S1d). Incorporating the SAM at that interface increases the G_C to 1.42±0.38 J.m^{-2}, but the fracture-surface characteristics in Fig. S2 remain unchanged. This ~31% increase in G_C is attributed to the SAM-induced adhesion mechanism described by Dai, *et al.*:[22] the cross-linked Si–O group anchors strongly to the ETL oxide surface, and the terminal I group bonds to the undercoordinated Pb in the MHP and also halogen-bonds to the I in the MHP. The c-TiO_2/m-TiO_2/MHP interface without the SAM is inherently tougher (G_C 2.27±0.55 J.m^{-2}) because it comprises of an interpenetrating nanocomposite of the mesoscopic TiO_2 scaffold and the MHP. The MHP side fracture surface appears rougher with hints of MHP microstructure (Fig. S3a), and little evidence of Ti in the corresponding XPS spectrum (Fig. S3b). Thus, the fracture path is not within the nanocomposite. The ETL side fracture surface (Fig. S3c) also appears rougher but it is quite different from the MHP side, suggesting that the fracture path is not well within the MHP capping layer either. Thus, the fracture path must be along the interface between the outer top surface of the mesoscopic TiO_2 scaffold and the bottom of the MHP capping layer (Fig. 1e). The incorporation of the SAM makes that interface even tougher (by ~35%), resulting in a G_C of 3.06±0.60 J.m^{-2}, which is comparable to the G_C of single-crystals of $MAPbI_3$ and $MAPbBr_3$ (~3 J.m^{-2}).[9] The fracture-surface characteristics in Fig. S4 remain unchanged, indicating that the same SAM-induced toughening mechanism is at play. Overall, there is about a three-fold enhancement in the G_C in going from c-TiO_2/MHP to c-TiO_2/m-TiO_2/SAM/MHP.

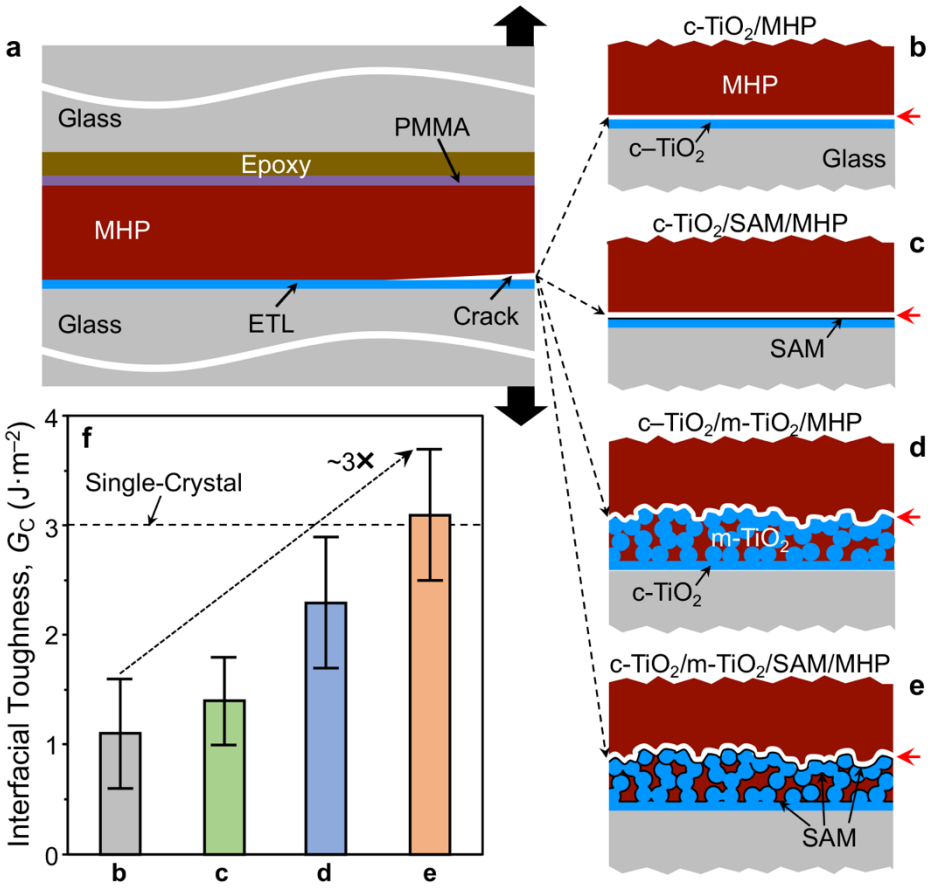

Figure 1. a) Schematic illustration of the DCB test (not to scale). Schematic illustrations of the four types of ETL/MHP interface regions indicating the fracture paths (white gaps and red arrows): b) c-TiO_2/MHP, c) c-TiO_2/SAM/MHP, d) c-TiO_2/m-TiO_2/MHP, and e) c-TiO_2/m-TiO_2/SAM/MHP. f) G_C values (average and standard deviation) of the four types of ETL/MHP interfaces..

2.2. Optoelectronic Properties and Small-Area PSCs

Figures 2a and 2b are steady-state and time-resolved (TR) photoluminescence (PL) spectra, respectively, of the four types of ETL/MHP interfaces. These data clearly show gains in the efficiency by which the photo-generated electrons are extracted by the m-TiO_2, compared to c-TiO_2, and it is further enhanced due to the presence of the SAM at the interface. The latter is attributed to the favorably oriented dipole induced by the silane-based SAM,[25] and it may not be related to the interfacial toughening effect. The bi-exponential fitting parameters of the TRPL data in Fig. 2b for the four types of interfaces are reported in Table S1. The average photocarrier lifetime (τ_{Avg}) decreases from 39 ns for the c-TiO_2/MHP to 18 ns for the c-TiO_2/m-TiO_2/MHP interface, and the SAM leads to a further reduction in the τ_{Avg} to 14 ns for the c-TiO_2/m-TiO_2/SAM/MHP interface.

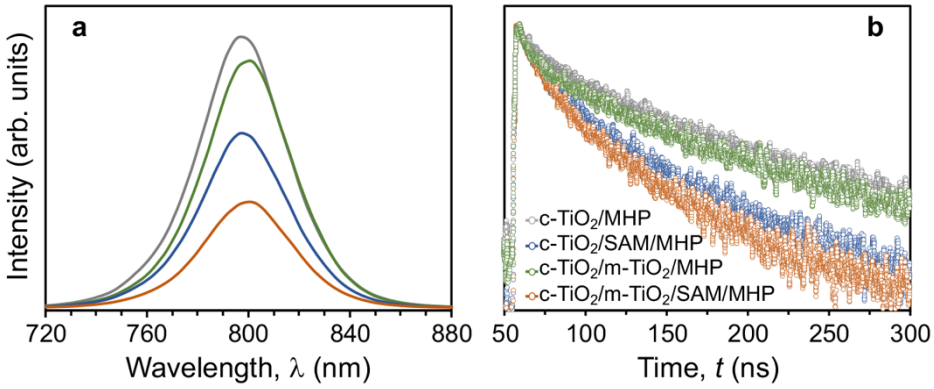

Figure 2. PL of the four types of ETL/MHP interfaces (laser excitation from MHP side): a) steady-state PL spectra and b) TRPL decay.

These four types of ETL/MHP interfaces were incorporated into PSCs. In all PSCs a LD MHP $(3\text{-CBA})_2PbI_4$; 3-CBA is 3-chlorobenzylamine) layer (~5 nm thickness) was grown *in situ* on the surface of the MHP thin film using a method described elsewhere,[23-24] followed by solution-deposition of a HTL (Li-doped Spiro OMeTAD) and thermal-evaporation of an Au thin-film electrode. Figure S5 presents the PV parameters data for PSCs (0.1 cm^2 active area) under AM 1.5G simulated 1 sun: short-circuit current density (J_{SC}), open-circuit voltage (V_{OC}), fill factor (FF), and PCE. A steady increase in all the average PV parameters in going from c-TiO_2/MHP to c-TiO_2/m-TiO_2/SAM/MHP is observed, which is, in part, attributed to the more efficient extraction of the photocarriers.

The rest of the study was focused on mesoscopic PSCs only, considering their high performance. Figures 3a and 3b present *J-V* responses of the 'champion' PSC with c-TiO_2/m-TiO_2/SAM/MHP interface, in reverse and forward scans showing minor hysteresis, and the corresponding external quantum efficiency (EQE) spectrum, respectively. The PV parameters extracted from these data are presented in the Fig. 3a inset, where the PCE has reached 24.12%. The integrated J_{SC} from the EQE spectrum of 25.09 $mA.cm^{-2}$ compares favorably with that from the *J-V* response. The corresponding stabilized PCE output at maximum power-point (MPP) of this PSC is presented in Figs. S6a, showing only 1.1% decay over 300 s.

Figure 3c presents operational-stability results for unencapsulated PSCs with c-TiO_2/m-TiO_2/SAM/MHP interface, together with a control PSC without the SAM (c-TiO_2/m-TiO_2/MHP), performed under continuous 1-sun illumination (MPP-tracking, flowing N_2, ~45 °C). There is initial transient behavior (up to ~220 h), followed by steady-state gradual degradation of the PCE. Linear fits to the steady-state PCE-degradation part are used to

calculate the T80, employing the extrapolation procedure from the literature,[22, 26] and it is described briefly in the Experimental Section. The extrapolated *T*80 for the control PSC is estimated at 4,485 h, whereas the PSC with SAM is remarkably stable with an extrapolated *T*80 of 18,334 h. This attests to the outsized effect of the incorporation of SAM in mesoscopic PSCs on their operational-stability.

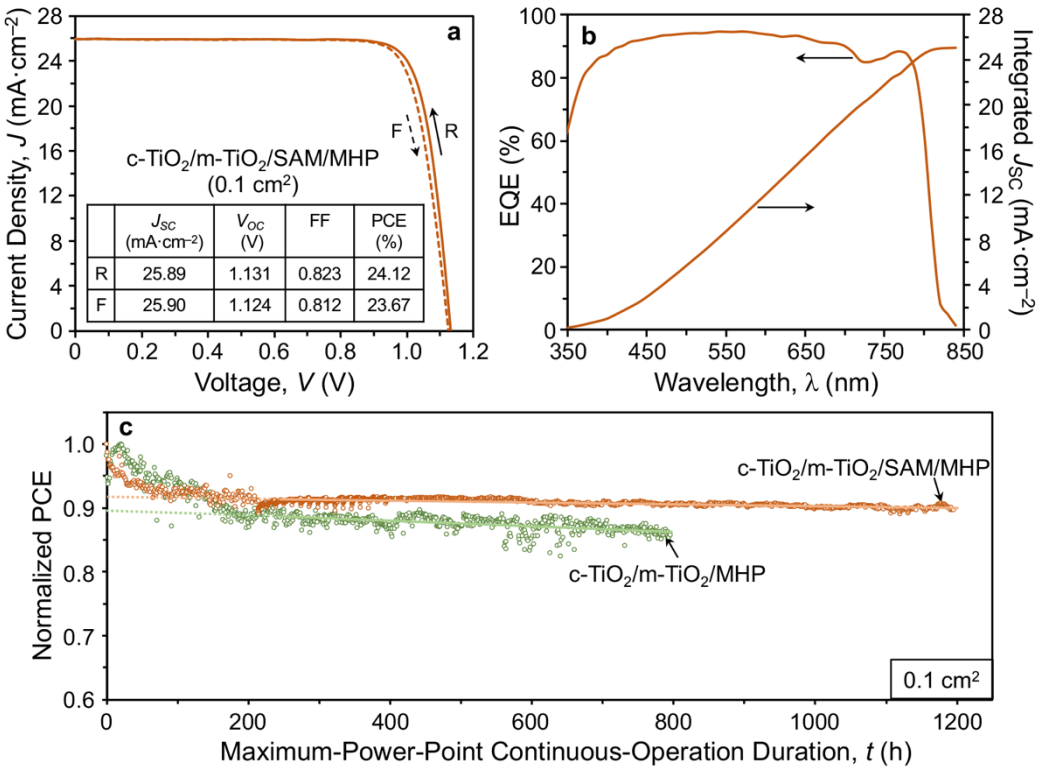

Figure 3. PV performance of 'champion' PSC (0.1 cm^2 active area) with c-TiO_2/m-TiO_2/SAM/MHP interface: a) *J-V* responses in forward and reverse scans (inset: PV parameters table) and b) EQE spectra and integrated J_{SC}. c) Operational-stability data for PSCs (0.1 cm^2 active area) with c-TiO_2/m-TiO_2/MHP and c-TiO_2/m-TiO_2/SAM/MHP interfaces. (Continuous 1-sun illumination, MPP-tracking, unencapsulated, ~45 °C, flowing N_2.) Dashed lines are linear fits to the steady-state degradation part of the data, which were used to estimate the extrapolated *T*80 lives.

2.3. Expanded-Area PSCs

To study the effect of up-scaling, control PSCs without the SAM (c-TiO_2/m-TiO_2/MHP; control) and PSCs with the SAM (c-TiO_2/m-TiO_2/SAM/MHP) of 1 cm^2 active area were fabricated. All PSCs have the same stack of (3-CBA)$_2$$PbI_4$/Spiro-OMeTAD/Au layers atop the MHP thin film. Figure S7 presents the PV parameters data for these PSCs under AM 1.5G simulated 1-sun: J_{SC}, V_{OC}, FF, and PCE. The presence of the SAM leads to an increase in all

the average PV parameters, consistent with what is observed in small-area PSCs (Fig. S5). Figures 4a and 4b present *J-V* responses and EQE spectrum, respectively, for the 'champion' expanded-area PSC. The PCE performance is reduced from 24.12% to 20.78% when the active area is increased from 0.1 cm^2 (Fig. 3a inset) to 1 cm^2 (Fig. 4a inset), which is primarily due to the lower FF, and the PSC becomes more hysteretic. The integrated J_{SC} from the EQE spectrum of 24.01 $mA.cm^{-2}$ compares favorably with that from the *J-V* response. The corresponding stabilized PCE output at MPP of this PSC is presented in Figs. S6b, showing only ~0.2% decay over 300 s.

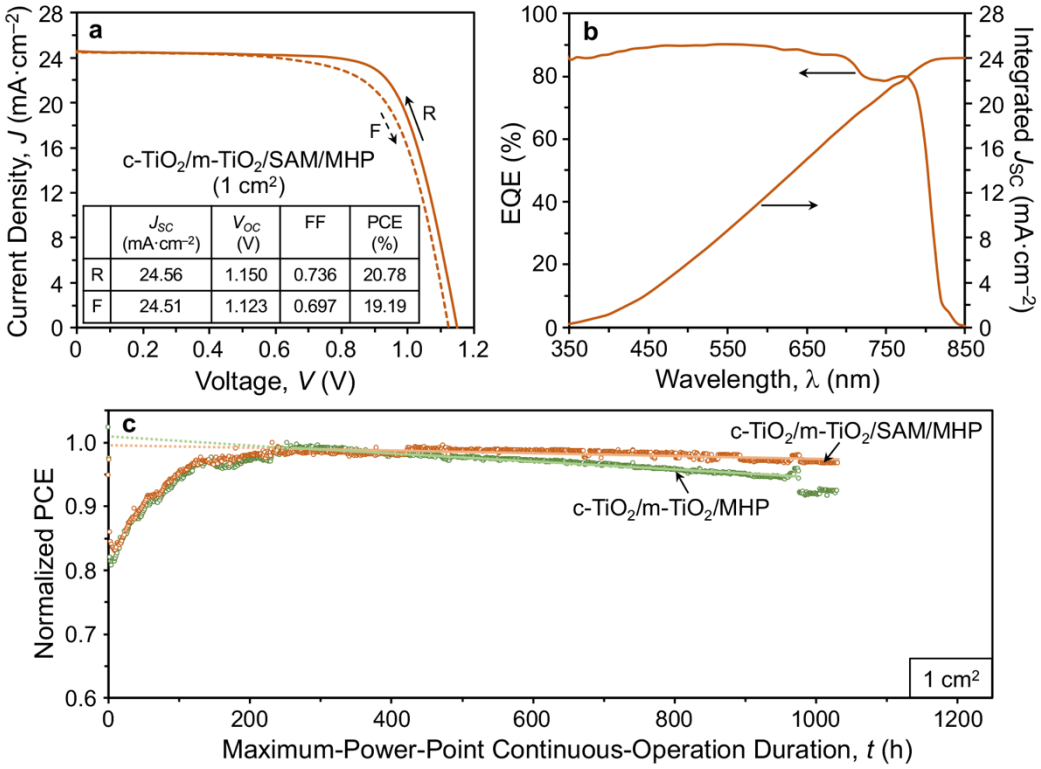

Figure 4. PV performance of 'champion' expanded-area PSC (1 active cm^2) with c-TiO_2/m-TiO_2/SAM/MHP interface: a) *J-V* responses in forward and reverse scans (inset: PV parameters table) and b) EQE spectra and integrated J_{SC}. c) Operational-stability data for PSCs (1 cm^2 active area) with c-TiO_2/m-TiO_2/MHP and c-TiO_2/m-TiO_2/SAM/MHP interfaces. (Continuous 1-sun illumination, MPP-tracking, unencapsulated, ~45 °C, flowing N_2.) Dashed lines are linear fits to the steady-state degradation part of the data, which were used to estimate the extrapolated *T*80 lives.

The operational-stability results for the expanded-area PSCs obtained using the same procedure and conditions as above are presented in Fig. 4c, which show a very rapid decay in the PCE initially, then recovery, followed by steady-state decay (after ~250 h). Thus, the procedure described earlier was applied to the steady-state-decay part of the data to estimate

an extrapolated *T*80 of 9,947 h for the PSC with SAM, compared to 2,885 h for the control PSC.

2.4. *Postmortem* Analysis

To understand and elucidate the degradation mechanisms, the operational-stability-tested 0.1-cm^2-active-area PSCs with c-TiO_2/m-TiO_2/MHP (control) and c-TiO_2/m-TiO_2/SAM/MHP interfaces were characterized in detail. Figures 5a and 5b present *J-V* responses (reverse scans) of a control PSC and a PSC with SAM, respectively, before the commencement of operational-stability testing and at the end of testing (for 1,000 h). The *J-V* responses clearly reinforce the beneficial effect of SAM on the operational-stability. However, cross-sectional SEM images of the corresponding tested PSCs Figs. 5c and 5d do not show any perceptible differences (addressed later).

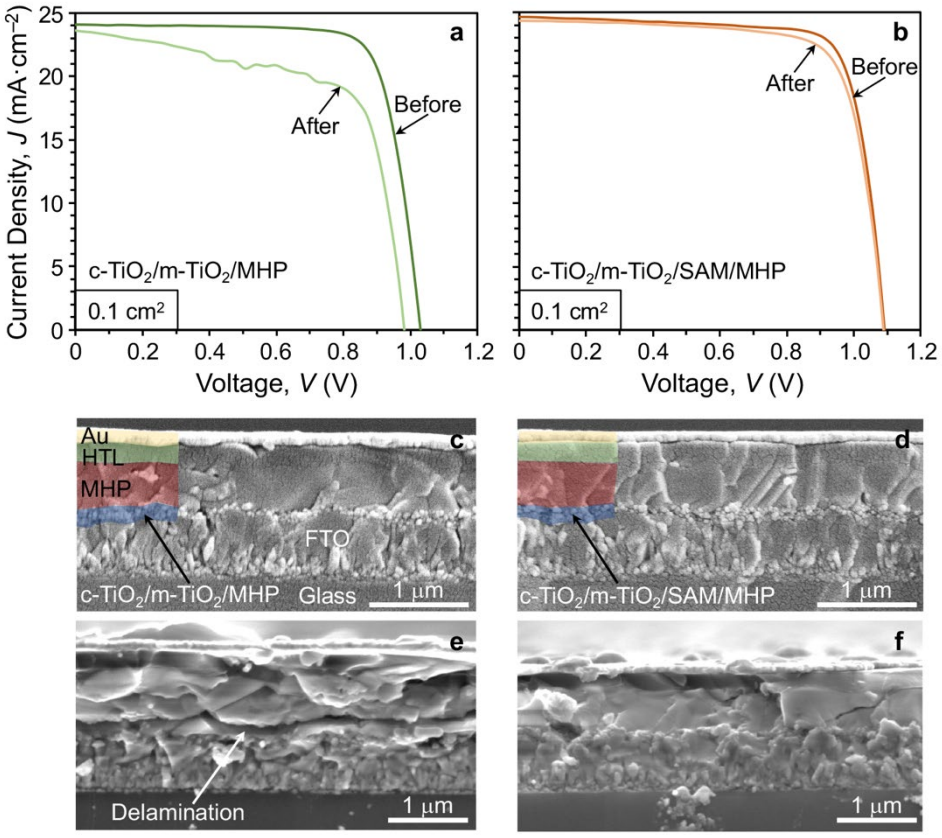

Figure 5. *J-V* responses (reverse scan) of PSCs with different ETL/MHP interfaces before and after operational-stability testing for 1,000 h: a) c-TiO_2/m-TiO_2/MHP and c-TiO_2/m-TiO_2/SAM/MHP. (Continuous 1-sun illumination, MPP-tracking, unencapsulated, ~45 °C, flowing N_2.) *Postmortem* cross-sectional SEM images of the 1,000-h operational-stability tested PSCs with different ETL/MHP interfaces: c) c-TiO_2/m-TiO_2/MHP and d) c-TiO_2/m-TiO_2/SAM/MHP. (Partial false coloring to demarcate the PSC layers.) *Postmortem* cross-sectional SEM images of the corresponding 1,000-h

operational-stability tested PSCs with additional 60-h testing in air: e) c-TiO_2/m-TiO_2/MHP and f) c-TiO_2/m-TiO_2/SAM/MHP.

To investigate this further, the tested PSCs were delaminated carefully using a procedure described in the Experimental Section, and the fracture surfaces were characterized. Figures 6a and 6d are SEM images of mating fracture surfaces of the control PSC, which look remarkably similar to the corresponding fracture surfaces from the toughness tests in Figs. S3a and S3b, suggesting fracture paths indicated in Figs. 1d and 1e, respectively. X-ray diffraction (XRD) patterns from the fracture surfaces in Figs. 6a and 6e are presented in Figs. 6c and 6g, respectively. Both show evidence of δ-$FAPbI_3$ and PbI_2, indicating chemical degradation of the MHP at that interface during the operation of that PSC, which appears to be, in part, responsible for the decay in its PV performance. The presence of δ-$FAPbI_3$ and PbI_2 is also indicated by the respective Pb 4*f* core-level XPS spectra in Figs. 6d and 6h, where the shift of the peaks for c-TiO_2/m-TiO_2/MHP (control) PSC higher binding energies is indicative of the presence of δ-$FAPbI_3$ [27] and PbI_2.[28] In order to investigate the degradation of the MHP/HTL top interface in these tested PSCs, the HTL and Au layers were removed carefully. From the XRD patterns and the XPS spectra in Figs. S8a and S8b, respectively, from the top surface of the MHP the amount of δ-$FAPbI_3$ and PbI_2 in both PSCs appears to be relatively small, which confirms that the top MHP/HTL interface is not as susceptible to degradation relative to the ETL/MHP bottom interface. This is typically the case in *n-i-p* PSCs tested under moisture-free (N_2) atmosphere, where the degradation of the MHP/HTL interface is more closely associated with the moisture in the environment.

In order to observe microscopic differences in the interfacial-degradation modes in PSCs with c-TiO_2/m-TiO_2/MHP and c-TiO_2/m-TiO_2/SAM/MHP, the PSCs stability-tested for 1,000 h were tested further for 60 h (1-sun, MPP-tracking) but under ambient air, instead of flowing N_2, to accelerate the degradation. Cross-sectional SEM images of the corresponding tested PSCs are presented in Figs. 5e and 5f, where more pronounced damage at the c-TiO_2/m-TiO_2/MHP interface (Fig. 5e), compared to the c-TiO_2/m-TiO_2/SAM/MHP interface (Fig. 5f), is clearly visible. Taken together, the results on *postmortem* analysis of the tested PSCs presented in Figs. 5, 6, and S8 highlight the beneficial effects of the SAM in reducing the extent of interfacial damage during the operation of those PSCs.

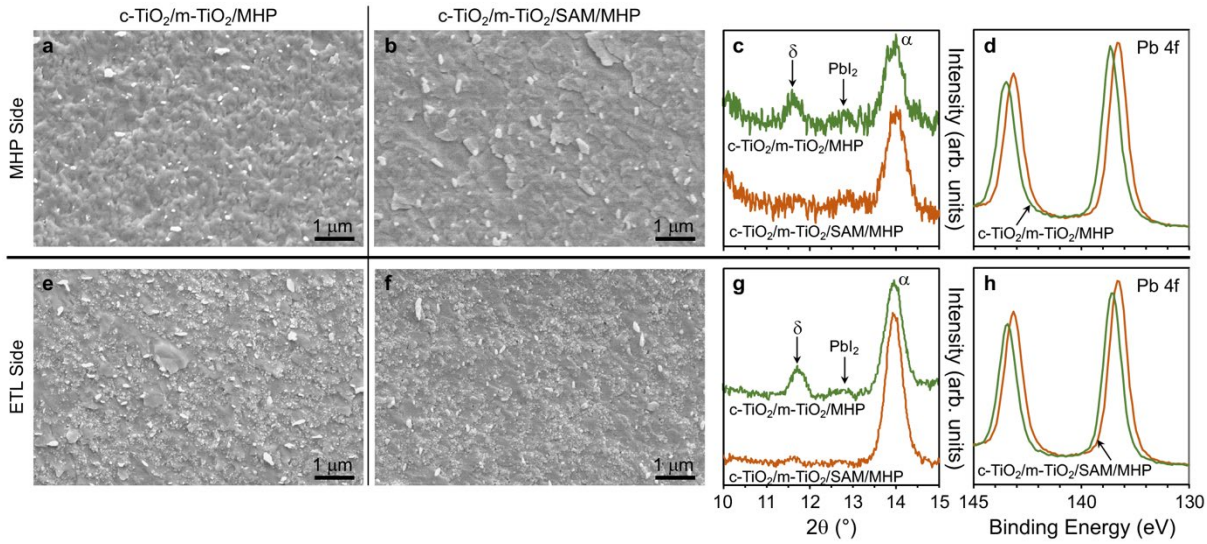

Figure 6. *Postmortem* SEM images of mating fracture surfaces (MHP side and ETL side) of the 1,000-h operational-stability tested PSCs from Figs. 5a-d with different ETL/MHP interfaces: a,e) c-TiO_2/m-TiO_2/MHP and b,f) c-TiO_2/m-TiO_2/SAM/MHP. Corresponding c,g) XRD patterns (α- and δ-$FAPbI_3$ MHP (001) and PbI_2 peaks marked) and d,h) XPS core-level spectra (Pb 4*f*) from the fracture surfaces.

Regarding the possible toughening mechanisms, the interpenetrating nanocomposite of MHP and TiO_2 at the interface in mesoscopic PSCs provides significantly higher contact area between MHP and TiO_2, which can promote photo-catalytic degradation of the MHP. However, the deposition of the surface-conformal SAM layer on the mesoscopic TiO_2 scaffold surfaces, both external and internal, before the MHP is infiltrated into the mesopores is likely to afford three beneficial effects. First, it is well known that alkoxysilane SAMs eliminate the OH groups that are ubiquitously present on metal (M) oxide surfaces *via* a condensation reaction to form Si–O–M anchoring covalent bonds at the surface;[29] trapped OH groups at the ETL/MHP interface are highly detrimental to the PSC performance.[22, 30] Second, the presence of SAM 'barrier' layer between the MHP and TiO_2 at all surfaces in the mesoscopic scaffold (illustrated schematically in Fig. 1e) is likely to reduce the propensity for the photocatalytic degradation of the MHP. Finally, any flaws (voids, cracks) that may nucleate at the ETL/MHP interface during the PSC operation are likely to have difficulty propagating further due to the high adhesion toughness (Fig. 1f). Thus, PSCs with c-TiO_2/m-TiO_2/SAM/MHP interface results in an unprecedented combination of enhanced mechanical reliability, operational-stability, and PCE. This opens up the possibility of exploring numerous combinations of mesoscopic ETL and SAMs for achieving high-performance PSCs of the future.

3. Summary

The combined effects of c-TiO_2 ETL without and with m-TiO_2 on top, and without and with an I-terminated silane SAM, on the mechanical behavior and the opto-electronic properties of the ETL/MHP interfaces were investigated. The performance and the operational-stability of the PSCs with these interfaces were evaluated. The interfacial toughness, G_C, was found to increase by almost three-fold in going from c-TiO_2 without SAM to m-TiO_2 with SAM. This is attributed to the synergistic effect of the m-TiO_2/MHP nanocomposite at the interface and the enhanced adhesion afforded by the I-terminated silane SAM. The combination of m-TiO_2 and SAM was also found to have a significant beneficial effect on the photocarriers extraction at the ETL/MHP interface. This resulted in 'champion' PSCs having PCE (reverse scan) of 24.12% and 20.78% for 0.1 cm^2 and 1 cm^2 active areas, respectively. These PSCs were also found to have long operational-stability lives, with extrapolated *T*80 of about 18,334 h and 9,947 h for 0.1 cm^2 and for 1 cm^2 active areas, respectively. *Postmortem* characterization and analysis of the operational-stability-tested PSCs revealed that the combination of m-TiO_2 and SAM results in reduced propensity for MHP degradation to PbI_2 and delamination cracking, which could be responsible for the long operational-stability. This study reinforces the utility of interfacial engineering in enhancing the PCE and durability of mesoscopic PSCs.

4. Experimental Section

Materials: All reagents were used as-received commercially without further purification, which include lead(II) iodide (PbI_2; 99%, Sigma Aldrich, USA), formamidinium iodide (FAI; >99.99%, Greatcell Solar Materials, Australia), lead(II) bromide ($PbBr_2$; ≥98%, Sigma Aldrich, USA), methylammonium bromide (MABr; >99.99%, Greatcell Solar Materials, Australia), cesium chloride (CsCl; 99.9%, Sigma Aldrich, USA), methylammonium chloride (MACl; >99.99%, Greatcell Solar Materials, Australia), N,N-dimethylformamide (DMF; 99.8%, anhydrous, Sigma Aldrich, USA), dimethyl sulfoxide (DMSO; ≥99.9%, anhydrous, Sigma Aldrich, USA), γ-butyrolactone (GBL; >99%, Sigma Aldrich, USA), 2-methoxyethanol (99.8%, anhydrous, Sigma Aldrich, USA), α-terpineol (Sigma Aldrich, USA), titanium diisopropoxide bis(acetylacetonate) ($Ti(acac)_2OiPr_2$; 75 wt.% in isopropanol, Sigma Aldrich, USA), titanium (IV) chloride ($TiCl_4$; ≥99.0%, Sigma Aldrich, USA), isopropanol (IPA; 99.5%, anhydrous, Sigma Aldrich, USA), diethyl ether (DEE; >99.9%, Sigma Aldrich, USA), bis(trifluoromethane)sulfonimide lithium salt (Li-TFSI; 99.95%, Sigma–Aldrich, USA), 4-tert-butylpyridine (tBP; 98%, Sigma Aldrich, USA), acetonitrile (99.8%, anhydrous, Sigma Aldrich, USA), chlorobenzene (99.8%, anhydrous, Sigma Aldrich, USA), spiro-OMeTAD (>99.8%, Lumtec, Taiwan), 3-iodopropyl)trimethoxysilane (≥95%, Sigma Aldrich, USA), TiO_2 nanoparticle paste (Sharechem, Korea), epoxy adhesive (Devcon, USA), and poly(methyl methacrylate) (PMMA; Sigma Aldrich,

USA).

Materials Synthesis: $MA_{0.02}FA_{0.98}Pb(I_{0.98}Br_{0.02})_3$ MHP single-crystals were synthesized for use as precursor material to control the purity and stoichiometry of the final MHP films. A mixture of 587.3 mg of PbI_2, 220.4 mg of FAI, 9.542 mg of $PbBr_2$, and 2.911 mg of MABr was dissolved in the mixture of 800 µL of GBL and 80 µL of 2-methoxyethanol at 70 °C, which was increased to 150 °C and then kept for 3 h at 150 °C. The black crystals were collected and washed with DEE and acetonitrile three times. The resulting MHP single-crystals were dried under vacuum for 3 h, and then stored in a N_2-filled glovebox for later use. All synthesis was performed in the N_2-filled glovebox.

3-CBAI for LD MHP was prepared using the method described elsewhere.[23-24] Briefly, 690 mg of 3-CBA was added to 10 mL of ethanol in a round-bottom flask. While the solution was being stirred in an ice-water bath, 1.1 g of HI solution was slowly added. The solution was stirred for 2 h to ensure complete reaction, and subsequently the solvent was removed using a rotary evaporator. The resulting 3-CBAI was obtained and washed with DEE, which was further dissolved in ethanol and recrystallized with DEE anti-solvent. The resulting 3-CBAI powder was dried in a vacuum oven at 50 °C for 24 h, and then stored in a N_2-filled glovebox for later use. All synthesis was performed in the N_2-filled glovebox.

Device Fabrication: Fluorinated-tin oxide (FTO)-coated soda-lime silicate glass substrates (TEC-8, 8 Ω/□, Pilkington, USA) was cleaned in the mixed solution of ethanol, acetone and deionized water (vol. ratio 1:1:1) by sonication for 30 min. The cleaned substrates were further cleaned by ultraviolet ozone (UVO) treatment for 30 min. A 50-nm thick compact TiO_2 (c-TiO_2) layer was deposited on the cleaned FTO substrate by sequential spin-coating of 0.15 and 0.3 M solution of $Ti(acac)_2OiPr_2$, followed by heat-treatment at 470 °C for 30 min in air. Mesoporous TiO_2 (m-TiO_2) was spin-coated at 2,000 rpm for 30 s on top of the c-TiO_2 using a diluted TiO_2 paste. The TiO_2 paste solution was prepared in 2-methoxyethanol/α-terpineol mixture (wt. ratio 3.5:1). The coated film was sintered at 470 °C for 60 min in air. Subsequently, c-TiO_2/m-TiO_2 substrate was immersed in a 20-mM aqueous solution of $TiCl_4$ solution at 70 °C for 20 min, followed by sintering at 470 °C for 30 min in the air. All processing was performed in ambient air.

SAM was deposited either after c-TiO_2 or after m-TiO_2 deposition by submerging the substrate in a 5 mM solution of $Si(OCH_3)_3(CH_2)_3I$ in mixture of isopropanol and DI water (vol. ratio 95:5) for 1 h. Subsequently, the substrates were dried under flowing dry N_2, and annealed at 100 °C for 5 min, followed by rinsing in IPA several times before drying under N_2 again. All processing was performed in ambient air.

The MHP precursor solution (1.6 M) was prepared by dissolving 1,008 mg of the synthesized single-crystals in a mixture of 890 µL DMF and 110 µL DMSO. To 1 ml of perovskite precursor 30 mol% (32.4 mg) of MACl and 3 mol% (8.08 mg) of CsCl. The precursor solution was stirred for 12 h at room temperature prior to deposition. The MHP layer was spin-coated on the prepared substrate at

1,000 rpm for 5 s followed by 5,000 rpm for 20 s, where 1 mL of DEE was dripped onto the rotating substrate. Subsequently, the film was annealed for 15 min at 150 °C under 17% RH. For the deposition of the LD MHP layer, the 3-CBAI solution (1 mg.mL^{-1} in IPA) was spin-coated at 3,000 rpm for 30 s, followed by annealing at 100 °C for 2 min. The spiro-OMeTAD layer was then spin-coated at 4,000 rpm for 30 s using a solution of 90 mg of spiro-OMeTAD, 39.5 μL of tBP, 23 μL of Li-TFSI (520 mg dissolved in 1 mL of acetonitrile) in 1 mL chlorobenzene. All processing was performed in a humidity-controlled glovebox. Finally, 80-nm thick Au electrode was deposited on the spiro-OMeTAD layer by thermal evaporation at an evaporation rate 0.1-0.4 Å.s^{-1}.

Characterization: A high-resolution SEM (Quattro ESEM, ThermoFisher Scientific, USA) was used to perform microstructural characterization. XRD characterization was performed using a high-resolution diffractometer (Discovery D8, Bruker, Germany) in ambient air. XPS characterization was performed using the K-Alpha X-ray photoelectron spectrometer (ThermoFisher, USA). PL and TRPL measurements were made using a 375 nm picosecond laser (PicoQuant LDH-D-C-375, Germany) as the excitation source in ambient air (films on FTO/ glass substrates). A long working-distance objective (10× numerical aperture of 0.28) was used to focus the excitation laser onto the sample, and simultaneously collect the PL signal. The PL was directed into a spectrograph (Ando Kymera 328i, UK), which was coupled with an electron-multiplying charge-coupled device (EMCCD; Andor iXon Life 888, UK) and a streak camera (C10910Hamamatsu, Japan) with the slow sweep unit.

Mechanical Testing: 'Sandwich' DCB specimens were prepared using the processes described above up to the deposition of the MHP film, but on bare soda-lime silicate glass substrates. A PMMA layer was deposited onto MHP surface for protection by spin-coating the PMMA solution (15 wt % in chlorobenzene), which was allowed to dry at room temperature for 1 h. Then, a thin layer of epoxy was applied onto the PMMA layer to 'glue' another cleaned glass superstrate on top. All the specimens were fabricated in ambient air.

The DCB specimens were tested in ambient air using a method described elsewhere.[4, 14, 22] Briefly, a planar pre-crack was introduced along the width (B=12.5 mm) dimension of the specimen by inserting a razor blade into the 'notch.' Initially, a pre-load of 0.2 N was applied to ensure a good contact between the specimen and the instrument. The cracked DCB specimens were then loaded in tension with a displacement rate of 3 μm.s^{-1} using a delaminator system (DTS, USA) until a well-defined planar crack at the ETL/MHP interface was obtained. The load (P) - displacement (Δ) response was recorded at all times. The specimen was then partially unloaded, and reloaded where the crack length, a, was estimated using the compliance method, in conjunction with the following relation:[14]

$$a = \left(\frac{d\Delta}{dP} * \frac{BEh^3}{8}\right)^{\frac{1}{3}} - 0.64h, \quad (1)$$

where B (=12.5 mm) and E (=70 GPa) are the width and the Young's modulus of the glass substrate, respectively, and h (=1 mm) is the half-thickness of the DCB specimen. The toughness, G_C, is then

given by the relation:[14]

$$G_C = \frac{12{P_C}^2 a^2}{B^2 E h^3}\left(1 + 0.64\frac{h}{a}\right)^2, \quad (2)$$

where P_C is the load at the onset of non-linearity in the P-Δ curve during the loading cycle. The loading-unloading cycles were repeated 2-3 times. Five measurements were made for each condition, and the average G_C and standard deviation are reported.

Photovoltaic Performance: The *J-V* responses of PSCs were measured in ambient air using a 2400 source meter (Keithley, USA) under simulated 1-sun illumination (AM 1.5G, 100 mW.cm^{-2}) which was generated using a class AAA simulator (Oriel Sol3A, Newport, USA) in air (~25 °C, ~25% RH). The light intensity was calibrated using a standard Si photodiode. Typically, the PSCs were measured in reverse scan (from V_{OC} to J_{SC}) and forward scan (from J_{SC} to V_{OC}) with a step size of 0.02 V and a delay time of 10 ms. A typical active area of 0.1 cm^2 or 1 cm^2 was defined using a nonreflective mask for *J-V* measurements. All the PSCs were measured without preconditioning such as light soaking and applied bias. The maximum power output stability of PSCs was measured by monitoring the stabilized current density output at the maximum power point bias (deduced from the reverse scan *J-V* curves). EQE of PSCs was measured using an internal quantum efficiency system (IQE-200B, Newport, USA) under irradiation by a 100 W xenon lamp.

Operational-stability testing was performed using an automated testing unit (Candlelight, Switzerland), where unencapsulated PSCs were loaded in a sealed chamber with a transparent quartz cover under continuous 1- sun intensity white LED illumination. A continuous flow of dry N_2 was supplied to the chamber to minimize the water and oxygen contents in the atmosphere (~45 °C, RH <5%). The light intensity was monitored and maintained throughout the test. The PSCs were measured with an MPP-tracking routine using a potentiostat. *J-V* curves were measured every hour, and the PSCs were biased at the MPP voltage by a standard perturb-and-observe algorithm.

Postmortem Characterization: Operational-stability tested PSCs were carefully prepared for *postmortem* characterization in ambient air. The top Au electrode was peeled off using scotch tape, and the spiro-OMeTAD layer was removed by spin-coating chlorobenzene. Subsequently, a 20 wt% PMMA solution was prepared in chlorobenzene and then spin-coated at 2,000 rpm for 60 s, and then a small amount of epoxy was applied uniformly. A fresh FTO-coated glass substrate was placed on the epoxy with the FTO side in contact, and gently pressed to facilitate uniform spreading to create a 'sandwich' specimen. A part of the specimen was cross-sectioned by scribing and fracturing, whereas the other half was delaminated carefully. Both the cross-sections and the delaminated-fracture surfaces were characterized.

Supporting Information

Supporting Information is available from the Wiley Online Library or from the

corresponding author.

Acknowledgements

The research at Brown University and NREL was funded by the U.S. Department of Energy (DOE) Office of Energy Efficiency and Renewable Energy under the Solar Energy Technology Office (Award No. DE-0009511). Additional support from research at Brown University was provided by the U.S. Office of Naval Research (Grant No. N00014-20-1-2574). The research at Yale University was primarily supported by U.S. National Science Foundation (Grant No. CHE-2305138). The views expressed in the article do not necessarily represent the views of the DOE or the U.S. Government.

Conflict of Interest

The authors declare no conflicting interests.

Data Availability Statement

All data generated or analyzed during this study are included in the published article and its Supporting Information.

References

[1] T. Miyasaka, *Perovskite Photovoltaics and Optoelectronics: From Fundamentals to Advanced Applications*, Wiley-VCH, Weinheim, Germany **2021**.

[2] X. Luo, X. Lin, F. Gao, Y. Zhao, X. Li, L. Zhan, Z. Qiu, J. Wang, C. Chen, L. Meng, X. Gao, Y. Zhang, Z. Huang, R. Fan, H. Liu, Y. Chen, X. Ren, J. Tang, C.-H. Chen, D. Yang, Y. Tu, X. Liu, D. Liu, Q. Zhao, J. You, J. Fang, Y. Wu, H. Han, X. Zhang, D. Zhao, F. Huang, H. Zhou, Y. Yuan, Q. Chen, Z. Wang, S. Liu, R. Zhu, J. Nakazaki, Y. Li, L. Han, *Sci. China Chem.* **2022**, 65, 2369.

[3] N. P. Padture, *MRS Bull.* **2023**, in press.

[4] N. Rolston, B. L. Watson, C. D. Bailie, M. D. McGehee, J. P. Bastos, R. Gehlhaar, J.-E. Kim, D. Vak, A. T. Mallajosyula, G. Gupta, A. D. Mohite, R. H. Dauskardt, *Extreme Mech. Lett.* **2016**, 9, 353.

[5] C. Ramirez, S. K. Yadavalli, H. F. Garces, Y. Zhou, N. P. Padture, *Scripta Mater.* **2018**, 150, 36.

[6] S. K. Yadavalli, Z. Dai, H. Zhou, Y. Zhou, N. P. Padture, *Acta Mater.* **2020**, 187, 112.

[7] M. Gutwald, N. Rolston, A. D. Printz, O. Zhao, H. Elmaraghi, Y. Ding, J. Zhang, R. H. Dauskardt, *Solar Energy Mater. Solar Cells* **2020**, 209, 110433.

[8] Q. Tu, D. Kim, M. Shyikh, M. G. Kanatzidis, *Matter* **2021**, 4, 2765.

[9] Z. Dai, M. C. Doyle, X. Liu, M. Hu, Q. Wang, C. E. Athanasiou, Y. Liu, S. Z. Liu, B. W. Sheldon, H. Gao, N. P. Padture, *Scripta Mater.* **2023**, 223, 115064.

[10] Z. Dai, N. P. Padture, *Nat. Energy* **2023**, in press.

[11] J. H. Yun, I. Lee, T.-S. Kim, M. J. Ko, J. Y. Kimae, H. J. Son, *J. Mater. Chem. A* **2015**, 3, 2176.

[12] B. L. Watson, N. Rolston, K. A. Bush, T. Leijtens, M. D. McGehee, R. H. Dauskardt, *ACS Appl. Mater. Interf.* **2016**, 8, 25896−25904.

[13] B. L. Watson, N. Rolston, K. A. Bush, L. Taleghani, R. H. Dauskardt, *J. Mater. Chem. A* **2017**, 5, 19267.

[14] N. Rolston, A.D. Printz, J.M. Tracy, H.C. Weerasinghe, D. Vak, L.J. Haur, A. Priyadarshi, N. Mathews, D.J. Slotcavage, M.D. McGehee, R.E. Kalan, K. Zielinski, R.L. Grimm, H. Tsai, W. Nie, A.D. Mohite, S. Gholipour, M. Saliba, M. Grätzel, R. H. Dauskardt, *Adv. Energy Mater.* **2018**, 8, 1702116.

[15] I. Lee, N. Rolston, P.-L. Brunner, R. H. Dauskardt, *ACS Appl. Mater. Interf.* **2019**, 11, 23757.

[16] H. Hwang, S. Park, J. H. Heo, W. Kim, H. Ahn, T.-S. Kim, S. H. Im, H. J. Son, *J. Power Sources* **2019**, 418, 167.

[17] S. Jeong, I. Lee, T.-S. Kim, J.-Y. Lee, *Adv. Mater. Interf.* **2020**, 7, 20001425.

[18] S. Song, E. Y. Park, B. S. Ma, D. J. Kim, H. H. Park, Y.Y. Kim, S. S. Shin, N. J. Jeon, T.-S. Kim, J. Seo, *Adv. Energy Mater.* **2021**, 11, 2003382.

[19] Z. Dai, S. K. Yadavalli, M. Hu, M. Chen, Y. Zhou, N. P. Padture, *Scripta Mater.* **2020**, 185, 47.

[20] M. Lyu, S. Park, H. Lee, B. S. Ma, S. H. Park, K.-H. Hong, H. Kim, T.-S. Kim, J. H. Noh, H. J. Son, N.-G. Park, *ACS Appl. Mater. Interf.* **2021**, 13, 35595.

[21] S. J. Sung, J. Im, G. Kim, C. S. Moon, J. J. Yoo, S. S. Shin, N. J. Jeon, B. S. Ma, D. J. Kim, T.-S. Kim, J. Seo, *Adv. Energy Mater.* **2022**, 12, 2200758.

[22] Z. Dai, S. K. Yadavalli, M. Chen, A. Abbaspourtamijani, Y. Qi, N. P. Padture, *Science* **2021**, 372, 618.

[23] Z. Dai, S. Li, X. Liu, M. Chen, C. E. Athanasiou, B. W. Sheldon, H. Gao, P. Guo, N. P. Padture, *Adv. Mater.* **2022**, 34, 2205301.

[24] Q. Dong, M. Chen, Y. Liu, F. T. Eickemeyer, W. Zhao, Z. Dai, Y. Yin, C. Jiang, J. Feng, S. Jin, S. Liu, S. M. Zakeeruddin, M. Grätzel, N. P. Padture, Y. Shi, *Joule* **2021**, 5, 1587.

[25] S. Y. Kim, S. J. Cho, S. E. Byeon, X. He, H. Y. Yoon, *Adv. Energy Mater.* **2020**, 10, 2002606.

[26] M. V. Khenkin, E. A. Katz, A. Abate, G. Bardizza, J. J. Berry, C. Brabec, F. Brunetti, V. Bulović, Q. Burlingame, A. D. Carlo, R. Cheacharoen, Y.-B. Cheng, A. Colsmann, S. Cros, K. Domanski, M. Dusza, C. J. Fell, S. R. Forrest, Y. Galagan, D. D. Girolamo, M. Grätzel, A. Hagfeldt, E. v. Hauff, H. Hoppe, J. Kettle, H. Köbler, M. S. Leite, S. Liu, Y.-L. Loo, J. M. Luther, C.-Q. Ma, M. Madsen, M. Manceau, M. Matheron, M. McGehee, R. Meitzner, M. K. Nazeeruddin, A. F. Nogueira, Ç. Odabaşı, A. Osherov, N.-G. Park, M. O. Reese, F. D. Rossi, M. Saliba, U. S. Schubert, H. J. Snaith, S. D. Stranks, W. Tress, P. A. Troshin, V. Turkovic, S. Veenstra, I. Visoly-Fisher, A. Walsh, T. Watson, H. Xie, R. Yıldırım, S. M. Zakeeruddin, K. Zhu, M. Lira-Cantu, *Nat. Energy* **2020**, 5, 35.

[27] I. Maeng, S. Lee, E. Q. Han, Y. Zhang, S. J. Oh, M. Nakamura, J.-H. Yun, L. Wang, Y.-K. Kwon, M.-C. Jung, *npg Asia Mater.* **2021**, 13, 75.

[28] I. S. Zhidkov, D. W. Boukhvalov, A. F. Akbulatov, L. A. Frolova, L. D. Finkelstein, A. I. Kukharenko, S. O. Cholakh, C.-C. Chueh, P. A. Troshin, E. Z. Kurmaev, *Nano Energy* **2021**, 79, 105421.

[29] L. Wang, U. S. Schubert, S. Hoeppener, *Chem. Soc. Rev.* **2021**, 50, 6507.

[30] G. Tumen-Ulzii, T. Matsushima, D. Klotz, M. R. Leyden, P. Wang, C. Qin, J.-W. Lee, S.-J. Lee, Y. Yang, C. Adachi, *Commun. Mater.* **2020**, 1, 31.